UCLA
UCLA Previously Published Works

Title
Single-Photon, Time-Gated, Phasor-Based Fluorescence Lifetime Imaging through Highly Scattering Medium

Authors
Ankri, Rinat
Basu, Arkaprabha
Ulku, Arin Can
et al.

Single-Photon, Time-Gated, Phasor-Based Fluorescence Lifetime Imaging through Highly Scattering Medium

Rinat Ankri*,†, **Arkaprabha Basu**†, **Arin Can Ulku**‡, **Claudio Bruschini**‡, **Edoardo Charbon**‡, **Shimon Weiss**†, **Xavier Michalet***,†

†Department of Chemistry & Biochemistry, UCLA, Los Angeles, California 90095, United States

‡School of Engineering, École Polytechnique Fédérale de Lausanne, Neuchâtel 1015, Switzerland

Abstract

Fluorescence lifetime imaging (FLI) is increasingly recognized as a powerful tool for biochemical and cellular investigations, including *in vivo* applications. Fluorescence lifetime is an intrinsic characteristic of any fluorescent dye which, to a large extent, does not depend on excitation intensity and signal level. In particular, it allows distinguishing dyes with similar emission spectra, offering additional multiplexing capabilities. However, *in vivo* FLI in the visible range is complicated by the contamination by (i) tissue autofluorescence, which decreases contrast, and by (ii) light scattering and absorption in tissues, which significantly reduce fluorescence intensity and modify the temporal profile of the signal. Here, we demonstrate how these issues can be accounted for and overcome, using a new time-gated single-photon avalanche diode array camera, SwissSPAD2, combined with phasor analysis to provide a simple and fast visual method for lifetime imaging. In particular, we show how phasor dispersion increases with increasing scattering and/or decreasing fluorescence intensity. Next, we show that as long as the fluorescence signal of interest is larger than the phantom autofluorescence, the presence of a distinct lifetime can be clearly identified with appropriate background correction. We use these results to demonstrate the detection of A459 cells expressing the fluorescent protein mCyRFP1 through highly scattering and autofluorescent phantom layers. These results showcase the possibility to perform FLI in challenging conditions, using standard, bright, visible fluorophore or fluorescence proteins.
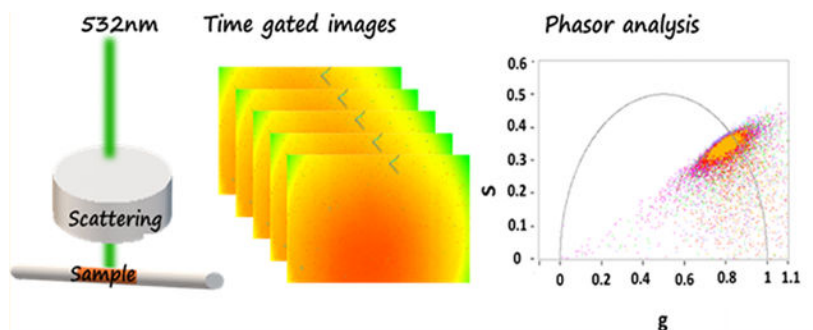
Graphical Abstract

Keywords

fluorescence lifetime imaging; phasor lifetime analysis; time-gated camera; single-photon detection; scattering medium

Fluorescence microscopy is an invaluable tool in biomedical investigations, which holds significant potential for various sensing applications, including probing tissue physiology, detecting early stages of disease *in vitro* and *in vivo*,[1,2] and sensing molecular concentrations of delivered pharmaceutical or intracellular fluorescent proteins.[3,4] However, its use in the visible wavelength range (400–650 nm) is limited to depths of no more than a few hundred micrometers inside the tissue, due to light scattering and absorption, as well as tissue autofluorescence (AF).[5,6] Many of these limitations are mitigated when using near-infrared (NIR)[4,7] or short-wave infrared (SWIR) emitting probes,[8] where light scattering and absorption by tissues is minimal, and endogenous fluorophores contribute negligible fluorescence.[7,9] Nonetheless, *in vivo* fluorescence imaging in the visible range has some advantages: ease of use, low cost, and a large selection of fluorescent dyes with good spectral separation as well as different lifetimes.[5,10] Conventional *in vivo* imaging methods in the visible range struggle to overcome tissue scattering and tissue absorption.[11–13] A tissue imaging technique based on visible illumination that is simple, fast, compact, portable, versatile, and inexpensive is therefore highly desirable.

Fluorescence lifetime imaging (FLI) is a powerful tool for noninvasive *in vitro* and *in vivo* biomolecular and cellular investigations.[14–17] Fluorescence lifetime is an intrinsic characteristic of any fluorescent dye, which, over a broad range of conditions, does not depend on excitation intensity and detected signal level. Moreover, it enables the separation of targeted dye signals from intrinsic tissue AF, provided their lifetimes differ sufficiently.[14] FLI can therefore provide enhanced sensitivity and contrast while allowing for lifetime-multiplexed detection using dyes with distinct lifetimes.

FLI can be measured in the frequency domain (frequency-modulated techniques) and the in time domain (time-resolved techniques).[18,19] Many time-domain FLI techniques use time-correlated single-photon counting (TCSPC), a technique generally used in scanning confocal setups[20] (with exceptions, see, e.g., ref 21), while the remainder use time-gating methods, which are generally used in wide-field geometries (with no scanning), as in this work. TCSPC methods record the arrival time of each photon after the excitation of a laser pulse and yield high-resolution histograms of arrival times, while time-gated FLI records the

fluorescence decay in a generally smaller number of integration windows ("gates") of finite width, providing a coarser representation of the fluorescence decay's temporal profile.[22,23]

Wide-field (parallel) data acquisition is highly desirable when imaging live cells or live animals, as it minimizes the temporal delay between data recorded in different regions of the field of view (FOV). It also has the advantage of dispensing with costly and complex scanning devices, even though it creates other challenges. In particular, the laser source needs to be sufficiently intense and present uniform illumination throughout the whole FOV. Specific to time-gated acquisition, all gates are acquired at a slightly different time, which requires the assumption that the sample remains quasi-static during the acquisition. This results in a trade-off to be made among fluorescence decay resolution (which gets better as the number of gates increases), signal-to-noise ratio (increasing with the integration time), and acquisition speed.[24]

In this paper, we use a recently introduced wide-field time-gated SPAD camera, SwissSPAD2,[23] characterized by low dark-count rate and fully configurable, high-resolution time-gating capabilities, allowing fluorescence lifetime imaging with picosecond time resolution and acquisition time as low as 2.6 ms per gate. We explore its ability to acquire FLI data through a tissue-like phantom and to enable distinguishing between extrinsic fluorescence and AF, through different phantom thicknesses mimicking skin tissue.

The resulting data were analyzed using the phasor approach,[25] providing a user-friendly graphical representation of fluorescence decays while still allowing quantitative analysis to be performed.[25,26] We show that phasor analysis of time-gated fluorescence of visible range dyes, loaded in glass capillaries and imaged through tissue-like phantom layers, can provide the necessary contrast for subcutaneous studies. Using the time-gated SwissSPAD2 camera, we were able to adjust the acquisition times to the dye concentration, avoiding any saturation or bleaching effects of the excited dye. We use different background analyses and standard deviation analysis to learn how and whether the lifetime changes with the intensity of the fluorescence, compared to the AF of the phantom, as well as with its scattering coefficient. We show that a simple computational background subtraction is sufficient for correct lifetime extraction when the fluorescence intensity is sufficiently high, but that for lower signals a phantom autofluorescence subtraction is preferable to extract the correct lifetime. We study the effect of increasing scattering coefficients on the dye's lifetime standard deviation (SDV) and values. Finally, we perform FLI of A549 cells expressing the fluorescent protein (FP) mCyRFP1 imaged through a 1.5 mm phantom layer and compare it to the FLI of control cells only exhibiting autofluorescence, to illustrate the ability of our approach to differentiate between both.

METHODS

Wide-Field FLI with SwissSPAD2.

A schematic description of the experimental setup is presented in Figure 1(a). A capillary (i.d.: 0.9 mm, o.d.: 1.2 mm) containing a dye solution (or a solution of suspended cells, see Figure 1(c) and details below) was held in a custom 3D-printed sample holder (see SI for details and CAD drawings). Tissue-like phantom layers (with varying thicknesses

of 0.5, 1, 1.5, 2, 3, and 5 mm) were inserted between the capillary and the microscope's objective lens (20×/0.4, LCPlanFl, Olympus). A 532 nm, 20 MHz repetition rate, pulsed laser with a pulse width full width at half-maximum (fwhm) < 100 ps (LDH-P-FA-530XL, Pico-Quant) was used as the excitation source. The incident power (<12 mW) on the sample was adjusted with the help of neutral density filters. The diffused emitted fluorescence was collected in an epi-illumination mode and imaged on the SwissSPAD2 (SS2) SPAD array mounted on the side camera port of the microscope. SS2 is composed of 472×276 single-photon avalanche diodes (SPAD).[23] The in-pixel time-gated architecture affords time-resolved photon counting at a maximum rate of 97 kfps (1-bit frames). The photon detection efficiency of the detector is 40% at 600 nm with a fill factor of 10.5% and dark count rate with a median value of 7.5 Hz/pixel. Overlapping gate images ($G = 117$, gate separation $\delta = 428.57$ ps) were used, while each experiment was using a different gate image acquisition time (4 to 400 ms), to account for different sample brightnesses and concentrations. Data files provided in the Supporting Information report the number n_G of gate "sequences" per 1-bit frame acquisition, and number b of 1-bit frame per gate image ($b = 255$ or 1020 depending on whether the gate images were 8-bit or 10-bit images). The total integration time, T_{int}, can be computed using the following formula:

$$T_{int} = G(n_G\theta_1 - \theta_0)b \qquad (1)$$

where $\theta_0 = 50$ ns and $\theta_1 = 400$ ns are firmware constants. Thus, for instance, the shortest value used in these measurements, $n_G = 5$, corresponds to a total integration time $T_{int} = 0.23$ s for 10-bit acquisition ($b = 1020$) of $G = 117$ gates covering the whole laser period of 50 ns (117×428.57 ps = 50.1 ns).

Dye Solution Preparation.

Cy3B (GE Healthcare, Waukesha, WI, USA) and ATTO 550 (ATTO-TECH) were prepared with double distilled water (ddH$_2$O), with estimated final concentrations of 10 μM (Cy3B) and 1.33 μM (ATTO 550), respectively, and loaded into capillaries (o.d.: 1.2 mm, i.d.: 0.9 mm, wall thickness: 150 μm, World Precise Instruments). The total sample volume within each capillary varied between experiments; however, the same FOV dimension was used for all samples and experiments.

Tissue-like Phantom Preparation.

Solid phantoms were prepared in order to mimic human tissues (brain, breast, soft tissues) as described next. Based on their optical properties (absorption coefficient: 0.17 mm^{-1}, scattering coefficient: ~0.75 mm^{-1}), 1 mm of these phantoms corresponds to 0.75 mm of human tissue.[27,28] The phantoms were prepared using India ink, as the absorbing component, and intralipid (IL) 20% (Lipofundin MCT/LCT 20%, B. Braun Melsungen AG, Germany), as the scattering component.[28–30] All phantoms contained the same ink (0.003%) and IL (0.75%) final concentrations (v/v), apart for the phantoms used in Figure 4, which contained increasing concentrations of IL (0.75, 1.5, 2, 4%). A 1% agarose powder (SeaKem LE Agarose, Lonza, USA) was added to the solution to form a gel. Briefly, the solutions were heated and mixed at a temperature of approximately 90 °C while the agarose powder was slowly added. The phantom solutions were stirred continuously to obtain high

uniformity. The mixture was then poured into a plastic syringe and stored in water until used. For each experiment, a slightly oversized slice of phantom was cut and placed on the phantom holder composed of a glass coverslip bottom taped to the 3D-printed spacer of appropriate thickness (0.5, 1, 1.5, 2, 3, or 5 mm), cut with a knife to achieve the desired thickness, and covered with another coverslip. This phantom slice was then slid under the sample (capillary) in the 3D-printed sample holder assembly.

Phantom and Sample Holder.

Round phantom molds with different thicknesses were designed using the free OpenSCAD software (files provided as additional data[31]) and 3D printed, providing five different phantom thickness options (0.5, 1, 1.5, 2, 3, and 5 mm, diameter 0.5 mm). A sample holder (illustrated in Figure 1b and, in more detail, in Figure S1) was similarly designed and 3D printed to load the phantom molds and position the capillary(ies) containing the sample(s) (dye solution or cells) at a fixed distance from the bottom of the phantom.

Cells.

Cell Culture.—A549 cells were cultured in Dulbecco's modified Eagle's medium (DMEM) containing 4.5 g/L D-glucose, 4 mM L-glutamine, and 110 mg/L sodium pyruvate supplemented with 10% fetal bovine serum (FBS) and 1% penicillin/streptomycin under standard conditions (37 °C and 5% CO_2). Total number of cells was 5–6 million.

Transfection.—Cultured A549 cells were transfected with 2.5 μg of mCyRFP1-C1 plasmid (a gift from Ryohei Yasuda, Addgene plasmid #84355)[32] using Lipofectamine 3000 as transfection reagent. Forty-eight hours post-transfection, cells were trypsinized, resuspended in phosphate-buffered saline (PBS), and centrifuged to collect the cell pellets. The suspensions were then injected into capillaries for FLI measurements.

In order to estimate the number of cells excited in the FOV, the total number of cells loaded within the capillary was divided by the total volume it occupied within the capillary, to give cell concentration per mm^3. Then, the irradiated volume of the capillary in the FOV (1.1 mm^2) was multiplied by this concentration to give the total number of cells in the FOV, resulting in ~300 000 cells.

Phasor Analysis.

Phasor analysis of the wide-field time-gated FLI data was performed as described previously[33,34] with minor modifications required by the presence of detector background and phantom autofluorescence, as described below.[35] All analyses were performed using AlliGator,[34] a freely available software developed in LabVIEW (National Instruments, Austin, TX, USA), dedicated to phasor analysis of time-gated data (download link provided in the SI). Briefly, the uncorrected, uncalibrated phasor ($g_{i,j}$, $s_{i,j}$) of each pixel of coordinates (i, j) in the image was calculated according to

$$\begin{cases} g_{i,j} = \dfrac{\sum_{k=1}^{G} F_{i,j}(t_k) \cos(2\pi f t_k)}{\sum_{k=1}^{N} F_{i,j}(t_k)} \\[4mm] s_{i,j} = \dfrac{\sum_{k=1}^{G} F_{i,j}(t_k) \sin(2\pi f t_k)}{\sum_{k=1}^{N} F_{i,j}(t_k)} \end{cases} \tag{2}$$

where f is the phasor harmonic (chosen in this study equal to the laser repetition rate = $1/T$), $k = 1, \ldots, G$ is the gate number, and $F_{i,j}(t_k)$ is the kth gate image value at pixel (i, j). When computing region of interest (ROI) phasor values, the $F_{i,j}(t_k)$ in eq 2 were replaced by the sum of all $F_{i,j}(t_k)$ in the ROI.

In practice, background-corrected phasors were used as described next.

Uncorrelated Background Correction.

Although the dark-count rate (DCR) of SS2 is very low (0.18 cps/μm^2), long integration can result in a significant amount of uncorrelated (i.e., constant) signal added to the contribution of fluorescence. Since the gate duration is constant, this contribution is equal for all gates and can be subtracted to recover the contribution of fluorescence only. Assuming a square-shaped gate of width W (a good approximation in these experiments) and a single-exponential decay with unknown amplitude A and lifetime τ (an approximation whose validity depends on which sample is considered), the unknown uncorrelated background contribution B (as well as the amplitude A and lifetime τ) can be computed by solving the system of equations obtained from three different points in the decay. The minimum and maximum fluorescence intensities, F_{min} and F_{max} (recorded for gates k_{min} and k_{max}, respectively), as well as the median intensity F_{med} (recorded for the median gate $k_{med} = 1/2(k_{min} + k_{max})$), can be expressed as

$$\begin{cases} F_{max} - B = A\dfrac{1 - e^{-W/\tau}}{1 - e^{-T/\tau}} \\[3mm] F_{min} - B = (F_{max} - B)e^{-(T-W)/\tau} \\[2mm] F_{med} - B = (F_{max} - B)e^{-(T-W)/2\tau} \end{cases} \tag{3}$$

which can be rewritten

$$\begin{cases} B = \dfrac{F_{min} - x F_{max}}{1 - x} \\[3mm] x = e^{-(T-W)/\tau} \end{cases} \tag{4}$$

where x is the solution of a quadratic equation, whose solution is

$$x = \left(\dfrac{F_{med} - F_{min}}{F_{max} - F_{med}}\right)^2 \tag{5}$$

The amplitude of the background-subtracted decay is equal to

$$A = \frac{F_{\text{max}} - F_{\text{min}}}{1 - x} \tag{6}$$

and the integrated background-subtracted signal (which can also be calculated by subtracting B from the decay and summing up the corrected gate signals) is given by

$$I_{\text{corr}} = A\frac{1 - e^{-W/\tau}}{1 - e^{-T/N\tau}} \sim A\left(1 - e^{-W/\tau}\right)\frac{N\tau}{T} \tag{7}$$

Using the uncorrelated background-corrected gate intensities $F_{i,j}(t_k) - B$ instead of $F_{i,j}(t_k)$ in eq 2 results in the uncorrelated background-corrected phasor used throughout this work.

Note that an estimate of the decay's lifetime can readily be obtained from x (eq 5):

$$\tau = \left(\frac{\ln x}{W - T}\right)^{-1} \tag{8}$$

The previous derivation is strictly valid only for single-exponential decay, but provides a reasonable approximation when the decay is dominated by a single-exponential component.

Phantom Autofluorescence Correction.

In the presence of a known phantom autofluorescence background (measured by recording the phantom in the absence of sample, in the exact same conditions of excitation intensity and integration time, $F_{i,j}^{\text{Phantom}}(t_k)$), an autofluorescence (and uncorrelated background)-corrected phasor can be computed, by replacing $F_{i,j}(t_k)$ by $F_{i,j}(t_k) - F_{i,j}^{\text{Phantom}}(t_k)$ in eq 2. This procedure is useful only if autofluorescence is not the dominant signal.

Photobleaching/Photobrightening Compensation.

In some cases, long acquisition times led to progressive decrease or increase of the signal, detected as a difference between the first and last gate intensity values, which, due to periodicity, should be identical. We used a simple exponential intensity correction model to compensate for this phenomenon. Note that in the absence of photobleaching or photobrightening, this correction has no effect on the recorded decay.

Phasor Calibration.

Background-corrected phasors computed as discussed still need to be calibrated using a reference sample with known lifetime τ_c, in order to account for the finite instrument response function (IRF),[34,36] as discussed next.

The theoretical phasor of the single-exponential decay calibration sample (located on the UC) is given by[25,37]

$$
\begin{cases}
\tilde{g}_c = \dfrac{1}{1 + (2\pi f \tau_c)^2} \\[3mm]
\tilde{s}_c = \dfrac{2\pi f \tau_c}{1 + (2\pi f \tau_c)^2}
\end{cases} \tag{9}
$$

Equivalently, treating the phasor (g, s) as a complex number z:

$$
\tilde{z}_c = \tilde{g}_c + i\tilde{s}_c = \tilde{m}_c e^{i\tilde{\varphi}_c} \tag{10}
$$

$\tilde{m}_c$ and $\tilde{\varphi}_c$ are the calibration phasor's modulus and phase, respectively, given by

$$
\begin{cases}
\tilde{\varphi}_c = \tan^{-1}(2\pi f \tau_c) \\[3mm]
\tilde{m}_c = \dfrac{1}{\sqrt{1 + (2\pi f \tau_c)^2}}
\end{cases} \tag{11}
$$

The reason for introducing these quantities is that the effect of a finite IRF on the phasor of any decay is to convolve the "pure" decay with the IRF, which, in the phasor representation, amounts to a simple multiplication by the IRF's complex phasor.

Calling z_c the measured (uncalibrated) phasor of the reference sample, the calibrated phasor $\tilde{z}$ of any measured sample is then given by

$$
\tilde{z} = z \frac{\tilde{z}_c}{z_c} \tag{12}
$$

or, using the modulus and phase notation:

$$
\begin{cases}
\tilde{\varphi} = \varphi + \tilde{\varphi}_c - \varphi_c \\[3mm]
\tilde{m} = m \dfrac{\tilde{m}_c}{m_c}
\end{cases} \tag{13}
$$

Because the detector temporal response is not perfectly uniform,[23] a local calibration phasor is preferable to fully correct for the detector's IRF spatial dependence.[38] The corresponding *phasor calibration map* consists of a set of calibration phasors $\{z_c(\vec{r}_i)\}$, $i = 1, \ldots, r$ where the $\{\vec{r}_i\}$ are uniformly distributed points across the detector (typically the centers of 4×4 pixel ROIs used in the analysis). As noted in ref 23, not using a phasor calibration map results in excess phase lifetime dispersion, which can hide more subtle effects such as dispersion due to shot noise or scattering. We used a high-intensity Cy3B sample imaged without phantom as our reference sample, the high intensity ensuring minimal contribution of shot noise (compared to the actual samples' shot noise) and no influence of scattering. The calibration lifetime used is the literature lifetime value $\tau = 2.8$ ns.[39,40]

Phase Lifetime Dispersion.

For any given sample (even one that is not characterized by a single-exponential decay), it is possible to compute a "phase lifetime" τ_φ from the calibrated phasor by inverting the first expression in eq 11:

$$\tau_\varphi = \frac{\tan \widetilde{\varphi}}{2\pi f} \tag{14}$$

(A "modulus lifetime" can also be computed using the inverse of the second expression in eq 11, but its usefulness is limited by the fact that it requires $\widetilde{m} \leq 1$, which is sometimes false due to noise.[25])

In order to study the respective contribution of signal intensity and scattering on the phase lifetime dispersion, a plot of phase lifetime versus intensity for a given sample is needed. This can be obtained in one of two ways:

- Several acquisitions with homogeneous intensity within the FOV, but recorded with different integration times.

- A single acquisition with inhomogeneous intensity within the FOV.

For samples observed behind a phantom layer, intensity inhomogeneity within the FOV is limited due to scattering, and therefore the first approach is necessary. For samples observed without phantoms, the nonuniformity of the illumination spot naturally creates fluorescence inhomogeneity throughout the FOV, and the second approach is the most efficient.

In either case, given a sample time-gated data set, phase lifetimes $\{\tau_{\varphi,i}\}$, $i = 1, \ldots R$, of nonoverlapping 4×4 pixel ROIs are calculated and a scatterplot of $\tau_{\varphi,i}$ versus I_i, the total intensity of ROI i, is computed.

In the first approach described above, the mean intensity of all ROIs, $\bar{I}$, is computed, while the histogram $h(\tau_\varphi)$ of $\{\tau_{\varphi,i}\}$ is fitted with a Gaussian distribution with standard deviation σ. This standard deviation is used as the measure of the phase lifetime dispersion for that average intensity. Repeating this operation with a sample of varying mean intensity $\bar{I}$, we obtain a function $\sigma(\bar{I})$ describing the dependence of the phase lifetime dispersion on average intensity.

In the second approach (nonuniform intensity throughout the FOV), the same type of scatterplot of $\tau_{\varphi,i}$ versus I_i is computed and then divided in "data slices" characterized by $s \Delta I \leq I_i < (s+1) \Delta I$, where ΔI is the slice's width, chosen such that each slice contains a sufficient number of data points to compute a meaningful standard deviation of the corresponding phase lifetimes (e.g., >100 data points). We thus obtain, with a single sample data set, a relation $\sigma(\bar{I}_s)$, where $\bar{I}_s = \left(s + \frac{1}{2}\right)\Delta I$ is the mean intensity of slice s as illustrated in Figure 2d. As discussed below, an inverse square root dependence $\sigma(\bar{I}) \sim \bar{I}^{-1/2}$ [36] indicates that the phase lifetime dispersion is dominated by shot noise,[36] while any departure from this behavior suggests that additional effects are at play.

RESULTS AND DISCUSSION

Effect of Increasing Phantom Thicknesses on the Phase Lifetime.

We first performed time-gated phasor FLI analysis of a bright Cy3B sample loaded in a thin glass capillary (concentration: 10 μM) placed behind various phantom thicknesses, in order to study the influence of scattering on the recorded signal intensity and measured fluorescence phase lifetime. Figure 2a shows the fluorescence intensity image of the Cy3B sample in the absence of phantom, as recorded with SS2 using an excitation power of 0.5 mW (measured before the objective lens) and a 0.25 s integration time. A scatterplot of a phasor of 4 × 4 pixel ROIs covering the whole FOV (see Supporting Information, Figure S1a) is shown in Figure 2b, after *uncorrelated background* (ucB) correction using eqs 4–8 and calibration with the phasor calibration map obtained with a separate, higher intensity Cy3B sample (see Methods). The corresponding phase lifetimes (eq 14) are plotted versus the 4 × 4 ROI intensities in Figure 2c, indicating that the phase lifetime variance increases for ROIs of lower intensity, while the phase lifetime itself shows a slight positive bias at low intensities. Figure 2d presents the phase lifetime SDV as a function of mean intensity per pixel obtained from the data shown in Figure 2c, fitted with a power law:

$$\sigma(\bar{I}) = A\bar{I}^{-\alpha} \tag{15}$$

where $\alpha = 0.45 \pm 0.02$, close to what is expected for a shot noise-limited observable.[36]

The same analysis (using the same calibration phasor) was then performed on the sample illuminated and observed through phantom layers of various thicknesses, to simulate measurement through various amounts of tissue.

In order to compensate for the attenuation of excitation and emission intensities due to absorption and scattering, increasing integration times were used as the phantom layer thickness was increased, in order to obtain comparable total collected signal for all measurements.[41] As an example, Figure 2e shows the image of the Cy3B sample observed behind a 1.5 mm thick phantom layer. Because of the increased integration time, the level of ucB increased proportionally (Supporting Information, Figure S3a) and had to be subtracted to recover the residual fluorescence signal. To do so, we used eqs 4–8, which assume that the recorded signal is described by a single-exponential decay integrated over a square gate. As we shall see later, this assumption is appropriate in this particular experiment, but need not be in general. Once corrected for ucB and normalized by the integration time, the data yield a recorded intensity that exhibits an exponential dependence on phantom thickness, with a characteristic length scale $d_0 = 0.77 \pm 0.27$ mm (see Supporting Information, Figure S4b).[23] In the absence of an analytical expression for the fluorescence intensity through a finite slab of scattering medium, we can but point at the similarity of this value with the literature value for the estimated scattering coefficient of this sample (0.75 mm^{-1}).[42]

Increased phantom thickness results in more photon scattering events, with a clearly observable effect of a more homogeneous intensity over the whole FOV (Figure 2e) by comparison to the initial, unevenly illuminated and emitting sample in the absence of phantom (Figure 2a). This intensity homogenization is accompanied by a reduced intensity

variance and a reduced phasor dispersion (compare Figure 2b and f). The corresponding phase lifetime variance[36] is correspondingly reduced (Figure 2g) and comparable to that obtained in the absence of a phantom layer (Figure 2h).

To disentangle the influence of intensity variance on phase lifetime variance from other potential sources of variance (e.g., scattering), we performed measurements with different phantom thicknesses, adjusting the integration time of each such as to keep the same averaged pixel intensity. If both phantom thickness and signal level contributed to the variance, fixing the intensity while varying the thickness should allow identifying any contribution from phantom thickness only. The result of this analysis is presented in Figure 2h, which shows phase lifetime (black) and phase lifetime SDV (red) for the same Cy3B sample as a function of phantom layer thickness. The measured phase lifetime is essentially constant (2.98 ± 0.07 ns), the small positive bias observed with increasing thickness being most likely due to phantom AF (see below), a phenomenon more clearly observed for low signal values in Figure 2c. The phase lifetime SDV is fairly constant for measurements behind phantoms ($\sigma_\tau = 25 \pm 4$ ps). Both results (constant phase lifetime and phase lifetime standard deviation) are the time domain equivalent of the phasor domain observations (e.g., Figure 2b,f), showing a measured decay insensitive to the amount of phantom material placed between the excitation source and sample and between sample and detector (Supporting Information, Figure S3).

Phantom Autofluorescence.

To investigate the possibility that the source of the observed phase lifetime bias for thick phantom is due to phantom AF, we performed similar measurements in the absence of sample. Figure 3 shows the result of this analysis, using identical integration time (24 s) and excitation power for all phantom thicknesses. The phantom's AF phasors appear fairly well represented by a single-exponential decay with lifetime $\tau_{ph} = 3.41 \pm 0.10$ ns superimposed to the ucB contribution of the detector (Figure 3a). The standard deviation of the phase lifetime also appears insensitive to the phantom's thickness (Figure 3b, black data points), consistent with the result obtained for the Cy3B sample observed through these different phantom thicknesses (presenting very similar fluorescence intensities, red data points in Figure 3b). Interestingly, the measured ucB-corrected count rates of all these phantoms are comparable (~1 kHz, Figure S4a) despite their very different thicknesses, suggesting that only a superficial layer (<0.5 mm) of the phantoms contributes most of the observed phantom AF. This observation is consistent with the fact that excitation and emission intensities are attenuated by absorption and scattering at larger depth.

With this information in hand, it is possible to revisit the Cy3B data and analyze the influence of phantom autofluorescence on the results shown in Figure 2. Indeed, because the fluorescence count rate decreased with increasing phantom thickness, integration time was increased to obtain a similar total signal for all samples, thus increasing the fractional contribution of the phantom autofluorescence to the total signal. Figure 3c represents this fraction, calculated as

$$\text{AF}\% = \frac{I_{\text{AF}}}{I_{\text{corr}}} \tag{16}$$

where I_{AF} is the phantom ucB-corrected autofluorescence count rate (reported in Supporting Information, Figure S4a), and I_{corr} is the ucB-corrected count rate (Supporting Information Figure S4b). The contribution of phantom autofluorescence increases steadily with phantom thickness, due to the reduction of the Cy3B sample's count rate, reaching 27% for the 5 mm phantom. The evolution of AF% is well fitted by a model assuming a constant contribution of phantom AF (rate I_{AF}) and an exponential dependence of the sample fluorescence count rate on phantom thickness, d:

$$\text{AF}\%(d) = \frac{I_{\text{AF}}}{I_{\text{AF}} + I_0 \exp\left(-\frac{d}{d_0}\right)} \tag{17}$$

with $d_0 = 1.18 \pm 0.09$ mm. Encouragingly, despite phantom AF, the phase lifetime of the Cy3B sample observed behind this same phantom is not markedly changed compared to measurements performed behind thinner phantoms (Figure 2), most likely because of (i) the low relative AF intensity and (ii) the small lifetime difference between the two species.

To further pinpoint the likely source of phantom AF, we recorded the fluorescence signal emitted by phantoms of identical thickness (0.5 mm) but composed of different IL concentrations and excited/recorded with identical illumination/integration time. As illustrated in Figure 3d, the AF phase lifetime did not depend on IL concentration. While the signal intensity increased linearly with concentration and quadrupled over the range of concentration used (Figure 3e), the phase lifetime SDV decreased by a factor of 2, as expected for a shot noise-limited signal. Since IL is used as a scattering agent, this AF component is an unfortunate side effect, which could possibly be alleviated using a different scattering component.

Testing the Limits of Phase Lifetime Measurements behind Phantoms.

To understand how phantom autofluorescence can affect the measured phase lifetime of samples with lower brightness, we looked at a dim sample of ATTO 550 (literature $\tau = 3.6$ ns). Figure 4a shows the phase lifetimes extracted from a series of measurements of the same ATTO 550 sample measured behind increasing phantom thicknesses, using the same integration time for all acquisitions (10 s). We compared two approaches for this calculation: (i) the approach used above for Cy3B, involving ucB-correction of the signal using eqs 4–8, which assume that the recorded signal is described by a single-exponential decay integrated over a square gate and neglects the presence of phantom AF (analytical background correction, ABC, red squares), and (ii) ucB and AF correction by direct subtraction of the phantom-only signal obtained in the series of experiments described in the previous section (file background correction, FBC, blue dots). Using the first analytical approach, the extracted phase lifetime (Figure 4a, red squares) becomes progressively closer to that of the phantom (Figure 4a, black triangles) as the phantom thickness increases. By contrast, using the phantom AF subtraction approach (Figure 4a, blue dots), the extracted phase lifetime remains fairly constant throughout the series, as the contribution of phantom

AF is removed. The price paid for this robustness is a significant increase of the phase lifetime standard deviation (Figure 4b, blue dots). This increase of the SDV is of course due to the decrease of the fluorescence signal detected through the phantom layers (Figure 4c), and thus reflects the shot noise effect discussed previously. Overall, it appears that as long as the ATTO 550 fluorescence signal is at least twice as large as the phantom AF (Figure 4c), the lifetime of that sample can be distinguished fairly robustly using only file background correction (see also in Supporting Information Figure S6).

The phase lifetime standard deviation can be used as a measure of the domain of validity of the analytical background subtraction approach, effective in the case of bright samples (Figure 2) but challenged in the case of dimmer samples (Figure 4). As indicated in Figure 4b, without AF subtraction (ABC, red curve), the SDV increases by a factor of 3.5 moving from a 0.5 mm to a 5 mm phantom, reaching the SDV measured for phantom AF (approximately independent of thickness). Based on the above measurements, this convergence of the sample's and AF's SDV can be used as a criterion to detect situations where analytical background subtraction becomes unreliable and should be replaced by phantom AF subtraction.

To check the influence of scattering on measurements of phase lifetimes close to the phantom AF lifetime, we performed similar measurements using 0.5 mm phantoms with varying intralipid concentration as done for Figure 3e,f. Figure 4d shows the result of these experiments: the recovered ATTO 550 phase lifetime is properly recovered no matter what IL concentration is used (red squares) and readily distinguished from phantom AF (black triangles). Note that because the ATTO 550 signal was high enough, analytical background correction was perfectly adequate for background correction.

In summary, the previous measurements show that in the presence of a fluorescence signal sufficiently larger than the phantom autofluorescence (independent from its thickness), reasonable estimation of the sample's fluorescence lifetime can be performed with appropriate background correction. While a purely analytical uncorrelated background subtraction approach can be used for bright samples, which can be useful when an AF measurement cannot be obtained, as might be the case for *in vivo* measurements, taking proper account of AF by subtracting a control data set corresponding to phantom only provides the most robust approach.

Live Cell Imaging behind Phantoms.

Having characterized the phase lifetime behavior of homogeneous fluorescent samples imaged through highly scattering medium, we used our time-gated approach to image a group of cells through similar phantom layers as a crude model for a tumor xenograft located subcutaneously. The basic question we asked was whether it is possible to distinguish unlabeled cells from cells expressing the fluorescent protein (FP) mCyRFP1,[32] with the goal of distinguishing cells targeted by a molecular marker (FP-expressing cells) and untargeted cells.

Figure 5 summarizes the result of these cell experiments. Figure 5a shows a schematic of the two adjacent capillaries containing the transfected and control cells, respectively, as

well as the FOV shown in Figure 5b,d. Figure 5b, which shows the fluorescence images of FP-expressing cells (left side) and control cells (right side) in the absence of phantom, also illustrates the larger brightness of the FP-expressing cells compared to the control cells (estimated number of cells in the FOV: 150 000 for each sample, excitation power: 12 mW, total integration time: 25 s). Figure 5d, by contrast, shows the fluorescence image of the same two capillaries shown in Figure 5b (FP-expressing cells adjacent to control cells) imaged through a 1.5 mm thick phantom layer, with a significant decrease in the fluorescence intensity. Unlike cells in the absence of phantom layer, the fluorescence from these cells is spread all over the frame, due to scattering in the phantom. Figure 5c and e show the phasor scatterplots of the two cell regions, after analytical ucB subtraction. In the absence of phantom (Figure 5c), the phasor scatterplot of the transfected cells (black) is characterized by a phase lifetime of 2.8 ns and is located in-between the phasor scatterplot of the control cells (red), characterized by a phase lifetime of 2.0 ns, and the location of the phasor of mCyRFP1 (black dot) based on its published lifetime (3.4 ns).[32] This suggests that the fluorescent signal from the transfected cell is in fact composed of a mixture of a significant fraction of cell AF signal superimposed to mCyRFP1 fluorescence.

In the presence of different phantom thicknesses, the plot of phase lifetimes extracted from the regions where the different samples were observed in the absence of phantom (Figure 5f), shows the following:

- A small increase of the phase lifetimes in the region under which cells expressing mCyRFP1 are located (phase lifetime change from 2.8 ns without phantom to 3.1 ns with a 1.5 mm phantom), despite marked decrease of the fluorescence intensity, similarly to what was observed for the dye samples in Figures 2 and 4.

- By contrast, the phase lifetimes in the region under which the control cells are located exhibit an increasing phase lifetime for increasing phantom thickness, becoming indistinguishable from that of the transfected cells and phantom AF, as expected for a weak fluorescent sample.

The phasor scatterplots of Figure 5e (1.5 mm phantom) illustrate this phenomenon in a complementary way. The phasor scatterplot of the region where the transfected cells were located (black scatterplot) shifts slightly along the line connecting pure mCyRFP1 (black dot on the UC) and control cell AF (red dot), corresponding to a minor additional contribution of the phantom AF to the total signal.

By contrast, the phasor scatterplot of the region where the control cells were located (red scatterplot) is now indistinguishable from that of the other region. This is due to complementary effects: on one hand, phantom AF has a larger influence on the weak cell AF signal; on the other hand, photons corresponding to the neighboring population of transfected cells (left region in Figure 5a,b,d), scattered throughout the phantom, now contribute some of their lifetime to the region on the right.

Note that the phase lifetime measured for the region where the transfected cells expressing mCyRFP1 are located, while similar to the phantom AF's lifetime, is clearly distinguishable from it for all phantom thicknesses (Figure 5e), thanks to its sufficient fluorescence intensity of the FP. This result is encouraging, as it says that mCyRFP1 fluorescence can be detected

even in the presence of phantom (or tissue) AF, as long as its signal is sufficient to not be overwhelmed by other intrinsic signals. This suggest that, in the case of a subcutaneous FP-expressing tumor xenograft, this extrinsic fluorescent signal might be detectable despite tissue AF (simulated here by the phantom and control cells) in favorable conditions of quantum yield, labeled cell concentrations, and tissue scattering properties or by limiting the excited region to dimensions comparable to the labeled cell region.

DISCUSSION

Optical imaging of fluorescent dyes has emerged as a powerful imaging method in preclinical applications due to the fast, noninvasive nature and quantitative results achieved by this approach. Interest in fluorescence-based techniques for clinical applications remains high due to their potential to target and detect specific tissues with high sensitivity, providing a fast, noninvasive, and quantitative readout. Due to the wide range of bright and biocompatible contrast agents and relatively low-cost instrumentation, the visible range of the electromagnetic spectrum would be attractive for clinical fluorescence-based imaging methods. However, a primary challenge with fluorescence-based imaging in the visible range is the development of detection methods that will overcome the major attenuation of light intensity in this region due to the high scattering and absorption of the tissue. Here, we demonstrated that phasor-based fluorescence lifetime imaging using a highly sensitive time-gated SPAD camera is capable of detecting fluorescent dyes and proteins emitting in the visible spectrum through a highly scattering tissue-like phantom. Despite the limitations of visible range imaging mentioned above, as well as the omnipresence of tissue autofluorescence, this work illustrates the potential of wide-field time-gated fluorescence lifetime imaging for this kind of application.

In particular, we showed that despite the presence of autofluorescence background, it is relatively straightforward to detect and identify the presence of a mass of FP-expressing cells characterized by a distinct lifetime behind up to 1.5 mm of phantom. FP have become a popular tool for live-cell and small-animal *in vivo* imaging, in particular for the study of localization, motility, and interaction of proteins in living cells,[43,44] mostly in the visible range. Their rapid rise as genetically manipulated imaging probes provides unique opportunities for real-time tracking of specific cells *in vivo*, enabling visualization of changes in target-gene promoter activity, tracking cellular movement in embryogenesis and inflammatory processes, monitoring migration of small para-sites within a host, and studying important aspects of cancer, such as tumor cell trafficking, invasion, metastasis, and angiogenesis.[45–48] Yet, in the case of *in vivo* applications, optical imaging of intact tissue does not provide cellular or intracellular resolution and hence, like PET, is limited to macro- or meso-localization of the fluorescent probe.[49–51] There is therefore a continuing interest in developing new probes and imaging systems for whole-body imaging. For instance, whole-animal imaging of FP-labeled tumors has been extended to NIR FP,[52,53] the tumors in these studies either being subcutaneous or consisting of several million cells in deep tissue. The very low tissue AF observed in this region of this spectrum will allow the method reported here to achieve a similar goal. On the instrument side, examples abound of recent developments to make the approach more practical. For example,[54] a macro-FLIM system for *in vivo* imaging purposes with a relatively high spatial resolution and molecular

specificity was recently demonstrated, enabling the detection of endogenous NAD(P)H fluorophores in tumor.[54] That work used a scanning TCSPC technique, which usually covers a relatively low scanning area, of 1×1 mm, but by placing the objects in the intermediate image plane of a confocal scanner, was able to achieve a larger FOV of more than 1 cm. A different approach based on a single-photon time-of-flight camera similar to SwissSPAD2 was recently demonstrated by Lyons et al.[55] that enables NIR imaging of objects embedded inside a strongly diffusive medium over more than 80 transport mean free paths,[55] although not involving fluorescence. Extending the results described here to the NIR, in particular the work involving the A549 cells transfected with mCyRFP1, demonstrating practical FLI through highly scattering medium, is the natural next step toward developing a simple and robust *in vivo* imaging method with improved contrast, sensitivity, and specificity for *in vivo* detection of FP or fluorescently labeled probes. Overall, SwissSPAD2, with its wide-field parallel imaging capabilities, should allow faster acquisition than TCSPC approaches than that mentioned above, while the phasor approach demonstrated here will make it computationally tractable, rapid, and practical.

Supplementary Material

Refer to Web version on PubMed Central for supplementary material.

ACKNOWLEDGMENTS

REFERENCES

(1). Valeur B Molecular fluorescence. digital Encyclopedia of Applied Physics 2009, 477–531.

(2). Kobayashi H; Ogawa M; Alford R; Choyke PL; Urano Y New strategies for fluorescent probe design in medical diagnostic imaging. Chem. Rev 2010, 110 (5), 2620–2640. [PubMed: 20000749]

(3). Zelphati O; Wang Y; Kitada S; Reed JC; Felgner PL; Corbeil J Intracellular delivery of proteins with a new lipid-mediated delivery system. J. Biol. Chem 2001, 276 (37), 35103–35110. [PubMed: 11447231]

(4). Fu AL; Tang R; Hardie J; Farkas ME; Rotello VM Promises and Pitfalls of Intracellular Delivery of Proteins. Bioconjugate Chem 2014, 25 (9), 1602–1608.

(5). Rice WL; Shcherbakova DM; Verkhusha VV; Kumar ATN In Vivo Tomographic Imaging of Deep-Seated Cancer Using Fluorescence Lifetime Contrast. Cancer Res 2015, 75 (7), 1236–1243. [PubMed: 25670171]

(6). Jacques SL Optical properties of biological tissues: a review. Phys. Med. Biol 2013, 58 (11), R37–R61. [PubMed: 23666068]

(7). Hong GS; Antaris AL; Dai HJ Near-infrared fluorophores for biomedical imaging. Nature Biomedical Engineering 2017, 1 (1), 0010.

(8). Thimsen E; Sadtler B; Berezin MY Shortwave-infrared (SWIR) emitters for biological imaging: a review of challenges and opportunities. Nanophotonics 2017, 6 (5), 1043–1054.

(9). Diao S; Hong GS; Antaris AL; Blackburn JL; Cheng K; Cheng Z; Dai HJ Biological imaging without autofluorescence in the second near-infrared region. Nano Res 2015, 8 (9), 3027–3034.

(10). Fixler D; Namer Y; Yishay Y; Deutsch M Influence of fluorescence anisotropy on fluorescence intensity and lifetime measurement: theory, simulations and experiments. IEEE Trans. Biomed. Eng 2006, 53 (6), 1141–1152. [PubMed: 16761841]

(11). Singh AK; Naik DN; Pedrini G; Takeda M; Osten W Exploiting scattering media for exploring 3D objects. Light: Sci. Appl 2017, 6 (2), No. e16219. [PubMed: 30167232]

(12). Jauregui-Sánchez Y; Clemente P; Lancis J; Tajahuerce E In Imaging through scattering media by Fourier filtering and single-pixel detection; Adaptive Optics and Wavefront Control for Biological Systems IV, International Society for Optics and Photonics: 2018; p 105020W.

(13). Xie XS; Zhuang HC; He HX; Xu XQ; Liang HW; Liu YK; Zhou JY Extended depth-resolved imaging through a thin scattering medium with PSF manipulation. Sci. Rep 2018, 8 (1), 4585. [PubMed: 29545584]

(14). Provenzano PP; Eliceiri KW; Keely PJ Multiphoton microscopy and fluorescence lifetime imaging microscopy (FLIM) to monitor metastasis and the tumor microenvironment. Clin. Exp. Metastasis 2009, 26 (4), 357–370. [PubMed: 18766302]

(15). Skala MC; Riching KM; Bird DK; Gendron-Fitzpatrick A; Eickhoff J; Eliceiri KW; Keely PJ; Ramanujam N In vivo multiphoton fluorescence lifetime imaging of protein-bound and free nicotinamide adenine dinucleotide in normal and precancerous epithelia. J. Biomed. Opt 2007, 12 (2), No. 024014. [PubMed: 17477729]

(16). Festy F; Ameer-Beg SM; Ng T; Suhling K Imaging proteins in vivo using fluorescence lifetime microscopy. Mol. BioSyst 2007, 3 (6), 381–391. [PubMed: 17533451]

(17). Yahav G; Barnoy E; Roth N; Turgeman L; Fixler D Reference-independent wide field fluorescence lifetime measurements using Frequency-Domain (FD) technique based on phase and amplitude crossing point. Journal of biophotonics 2017, 10 (9), 1198–1207. [PubMed: 27774782]

(18). Lakowicz JR; Szmacinski H; Nowaczyk K; Johnson ML Fluorescence Lifetime Imaging of Calcium Using Quin-2. Cell Calcium 1992, 13 (3), 131–147. [PubMed: 1576634]

(19). Yahav G; Gershanov S; Salmon-Divon M; Ben-Zvi H; Mircus G; Goldenberg-Cohen N; Fixler D Pathogen Detection Using Frequency Domain Fluorescent Lifetime Measurements. IEEE Trans. Biomed. Eng 2018, 65 (12), 2731–2741. [PubMed: 29993446]

(20). Becker W Advanced Time-Correlated Single Photon Couting Techniques; Springer: Berlin, 2005.

(21). Michalet X; Pinaud FF; Bentolila LA; Tsay JM; Doose S; Li JJ; Sundaresan G; Wu AM; Gambhir SS; Weiss S Quantum dots for live cells, in vivo imaging and diagnostics. Science 2005, 307 (5709), 538–44. [PubMed: 15681376]

(22). Ebrecht R; Don Paul C; Wouters FS Fluorescence lifetime imaging microscopy in the medical sciences. Protoplasma 2014, 251 (2), 293–305. [PubMed: 24390249]

(23). Ulku AC; Bruschini C; Antolovic IM; Kuo Y; Ankri R; Weiss S; Michalet X; Charbon E, A 512×512 SPAD Image Sensor with Integrated Gating for Widefield FLIM. IEEE J. Sel. Top. Quantum Electron 2019, 25, 1.

(24). Becker W Fluorescence lifetime imaging by multi-dimensional time correlated single photon counting. Medical Photonics 2015, 27, 41–61.

(25). Digman MA; Caiolfa VR; Zamai M; Gratton E The phasor approach to fluorescence lifetime imaging analysis. Biophys. J 2008, 94 (2), L14–L16. [PubMed: 17981902]

(26). Stringari C; Cinquin A; Cinquin O; Digman MA; Donovan PJ; Gratton E Phasor approach to fluorescence lifetime microscopy distinguishes different metabolic states of germ cells in a live tissue. Proc. Natl. Acad. Sci. U. S. A 2011, 108 (33), 13582–7. [PubMed: 21808026]

(27). Sandell JL; Zhu TC A review of in-vivo optical properties of human tissues and its impact on PDT. J. Journal of biophotonics 2011, 4 (11–12), 773–787. [PubMed: 22167862]

(28). Jacques SL Optical properties of biological tissues: a review. Phys. Med. Biol 2013, 58 (11), R37. [PubMed: 23666068]

(29). Dam JS; Pedersen CB; Dalgaard T; Fabricius PE; Aruna P; Andersson-Engels S Fiber-optic probe for noninvasive real-time determination of tissue optical properties at multiple wavelengths. Appl. Opt 2001, 40 (7), 1155–1164. [PubMed: 18357101]

(30). Cubeddu R; Pifferi A; Taroni P; Torricelli A; Valentini G A solid tissue phantom for photon migration studies. Phys. Med. Biol 1997, 42 (10), 1971–1979. [PubMed: 9364593]

(31). Ankri R; Basu A; Ulku AC; Charbon E; Weiss S; Michalet X Supporting Data for Single Photon, Time-Gated, Phasor-based Fluorescence Lifetime Imaging Through Highly Scattering Medium. Figshare, 2019.

(32). Laviv T; Kim BB; Chu J; Lam AJ; Lin MZ; Yasuda R Simultaneous dual-color fluorescence lifetime imaging with novel red-shifted fluorescent proteins. Nat. Methods 2016, 13 (12), 989–992. [PubMed: 27798609]

(33). Fereidouni F; Esposito A; Blab G; Gerritsen H. J. J. o. m. A modified phasor approach for analyzing time-gated fluorescence lifetime images. J. Microsc 2011, 244 (3), 248–258. [PubMed: 21933184]

(34). Chen S-J; Sinsuebphon N; Barroso M; Intes X; Michalet X In AlliGator: A Phasor Computational Platform for Fast in Vivo Lifetime Analysis; Optical Molecular Probes, Imaging and Drug Delivery, Optical Society of America: 2017; p OmTu2D. 2.

(35). Clayton AH; Hanley QS; Verveer PJ Graphical representation and multicomponent analysis of single-frequency fluorescence lifetime imaging microscopy data. J. Microsc 2004, 213, 1–5. [PubMed: 14678506]

(36). Colyer RA; Lee C; Gratton E A novel fluorescence lifetime imaging system that optimizes photon efficiency. Microsc. Res. Tech 2008, 71 (3), 201–213. [PubMed: 18008362]

(37). Chen SJ; Sinsuebphon N; Rudkouskaya A; Barroso M; Intes X; Michalet X In vitro and in vivo phasor analysis of stoichiometry and pharmacokinetics using short-lifetime near-infrared dyes and time-gated imaging. J. Biophotonics 2018, 12 (3), No. e201800185. [PubMed: 30421551]

(38). Ulku A; Ardelean A; Antolovic M; Weiss S; Charbon E; Bruschini C; Michalet X Wide-field time-gated SPAD imager for phasor-based FLIM applications. BioXriv 2019, 687277.

(39). Cooper M; Ebner A; Briggs M; Burrows M; Gardner N; Richardson R; West R Cy3B: improving the performance of cyanine dyes. J. Fluoresc 2004, 14 (2), 145–150. [PubMed: 15615040]

(40). Sanborn ME; Connolly BK; Gurunathan K; Levitus M Fluorescence properties and photophysics of the sulfoindocyanine Cy3 linked covalently to DNA. J. Phys. Chem. B 2007, 111 (37), 11064–11074. [PubMed: 17718469]

(41). Gandjbakhche AH; Weiss GH; Bonner RF; Nossal R Photon Path-Length Distributions for Transmission through Optically Turbid Slabs. Phys. Rev. E: Stat. Phys., Plasmas, Fluids, Relat. Interdiscip. Top 1993, 48 (2), 810–818.

(42). Shahin A; El-Daher MS; Bachir W. J. P. L. o. P., Determination of the optical properties of Intralipid 20% over a broadband spectrum. Photonics Lett. Pol 2018, 10 (4), 124–126.

(43). Cranfill PJ; Sell BR; Baird MA; Allen JR; Lavagnino Z; de Gruiter HM; Kremers GJ; Davidson MW; Ustione A; Piston DW Quantitative assessment of fluorescent proteins. Nat. Methods 2016, 13 (7), 557–62. [PubMed: 27240257]

(44). Bajar BT; Wang ES; Lam AJ; Kim BB; Jacobs CL; Howe ES; Davidson MW; Lin MZ; Chu J Improving brightness and photostability of green and red fluorescent proteins for live cell imaging and FRET reporting. Sci. Rep 2016, 6, 20889. [PubMed: 26879144]

(45). Hoffman RM Advantages of multi-color fluorescent proteins for whole-body and in vivo cellular imaging. J. Biomed. Opt 2005, 10 (4), 41202. [PubMed: 16178626]

(46). Passamaneck YJ; Di Gregorio A; Papaioannou VE; Hadjantonakis AK Live imaging of fluorescent proteins in chordate embryos: from ascidians to mice. Microsc. Res. Tech 2006, 69 (3), 160–7. [PubMed: 16538622]

(47). Stewart CN Go with the glow: fluorescent proteins to light transgenic organisms. Trends Biotechnol 2006, 24 (4), 155–162. [PubMed: 16488034]

(48). Wacker SA; Oswald F; Wiedenmann J; Knochel W A green to red photoconvertible protein as an analyzing tool for early vertebrate development. Dev. Dyn 2007, 236 (2), 473–480. [PubMed: 16964606]

(49). Chen J; Venugopal V; Lesage F; Intes X Time-resolved diffuse optical tomography with patterned-light illumination and detection. Opt. Lett 2010, 35 (13), 2121–2123. [PubMed: 20596166]

(50). Ozturk MS; Rohrbach D; Sunar U; Intes X Mesoscopic fluorescence tomography of a photosensitizer (HPPH) 3D biodistribution in skin cancer. Acad. Radiol 2014, 21 (2), 271–80. [PubMed: 24439340]

(51). Ozturk MS; Chen CW; Ji R; Zhao L; Nguyen BN; Fisher JP; Chen Y; Intes X Mesoscopic Fluorescence Molecular Tomography for Evaluating Engineered Tissues. Ann. Biomed. Eng 2016, 44 (3), 667–79. [PubMed: 26645079]

(52). Deliolanis NC; Ale A; Morscher S; Burton NC; Schaefer K; Radrich K; Razansky D; Ntziachristos V Deep-tissue reporter-gene imaging with fluorescence and optoacoustic tomography: a performance overview. Mol. Imaging Biol 2014, 16 (5), 652–60. [PubMed: 24609633]

(53). Shcherbakova DM; Baloban M; Verkhusha VV Near-infrared fluorescent proteins engineered from bacterial phytochromes. Curr. Opin. Chem. Biol 2015, 27, 52–63. [PubMed: 26115447]

(54). Shcheslavskiy VI; Shirmanova MV; Dudenkova VV; Lukyanov KA; Gavrina AI; Shumilova AV; Zagaynova E; Becker W Fluorescence time-resolved macroimaging. Opt. Lett 2018, 43 (13), 3152–3155. [PubMed: 29957804]

(55). Lyons A; Tonolini F; Boccolini A; Repetti A; Henderson R; Wiaux Y; Faccio D Computational time-of-flight diffuse optical tomography. Nat. Photonics 2019, 13, 1.
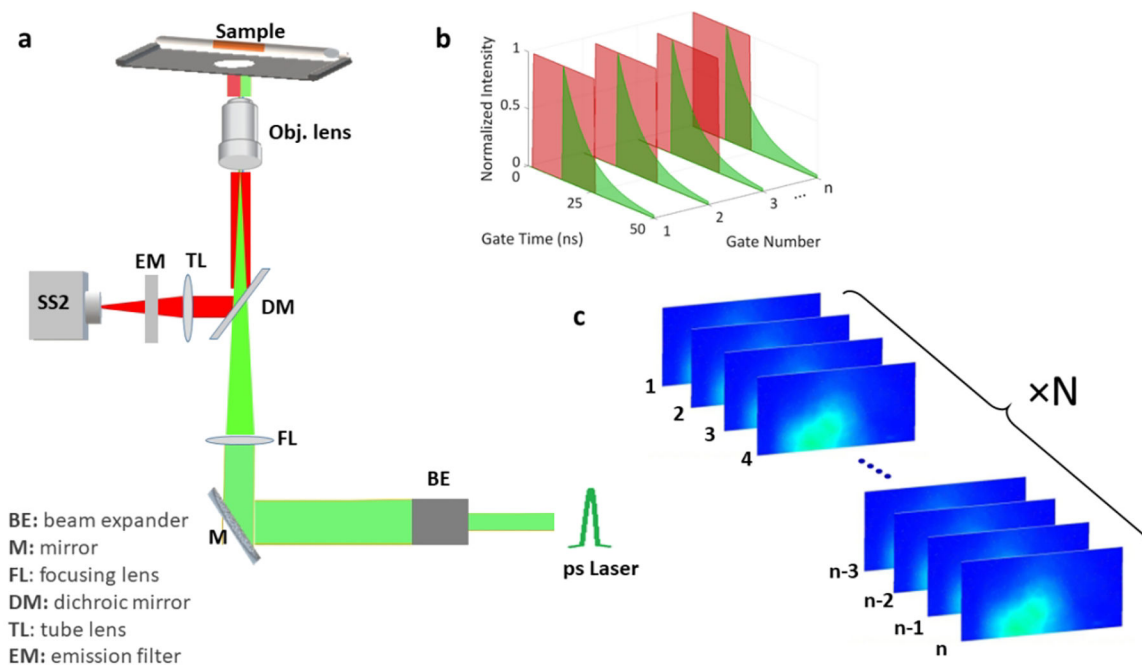
Figure 1.
Schematic description of the wide-field time-gated FLI setup. (a) FLI setup. The sample was illuminated with a 532 nm picosecond laser, and emitted fluorescence was captured using the time-gated SwissSPAD2 (SS2) SPAD array (512 × 256 pixels). Excitation power varied for the different samples, but for all samples behind phantoms we used an incident excitation power of 12 mW. (b) Conceptual illustration of time gating in SwissSPAD2. The delay between subsequent gate positions is a small fraction of the gate width, resulting in overlapping gates. The decay is composed of 125 such gates. (c) For some samples, multiple series (dashed box) of 125 gate images (n_i = number of images for all series) were recorded successively, in order to avoid significant bleaching during recording. Variable numbers of such series were summed postacquisition to obtain the desired total signal intensity.
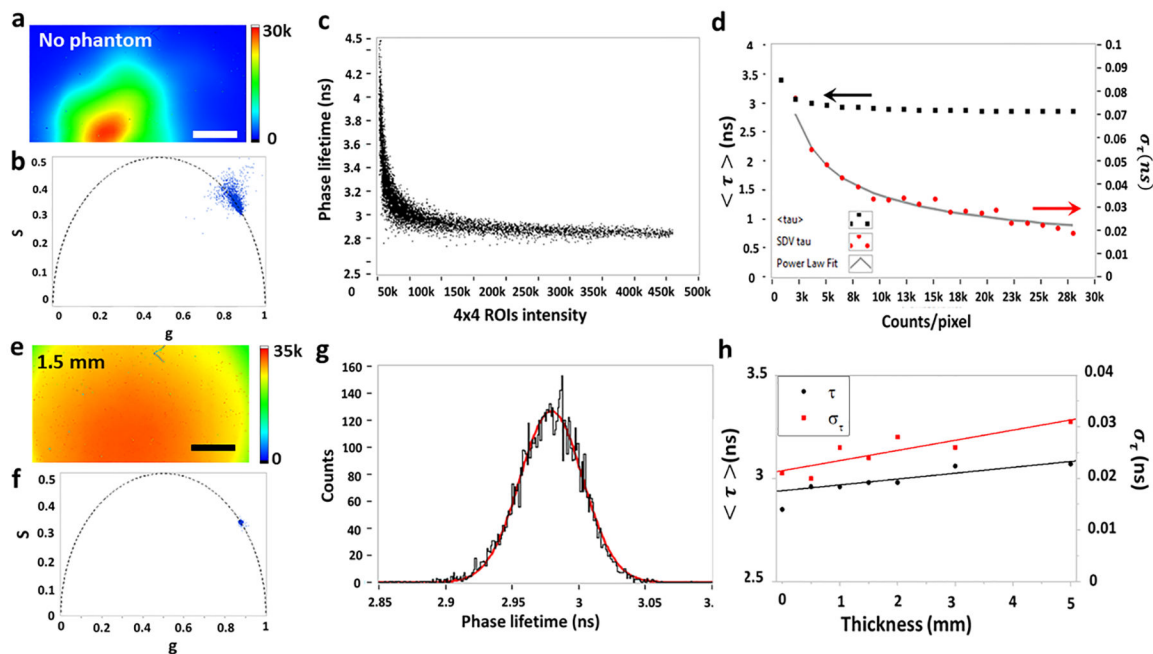
Figure 2.

Phase lifetime analysis of Cy3B behind different phantom thicknesses. (a and e) Color-coded intensity images of the Cy3B sample observed behind no phantom or a 1.5 mm phantom, respectively. (e) shows a more homogeneous fluorescence intensity, due to scattering in the phantom. Scale bar is 160 μm. (b and f) Phasor scatterplots for the data sets shown in (a) and (e), respectively, calculated using 4×4 pixel ROIs covering the full FOV of each image (see Figure S2a in the Supporting Information for details). The phasors are calibrated using the known Cy3B lifetime (τ = 2.8 ns) and a phasor harmonic frequency f = 20 MHz. (c) Scatterplot of phase lifetime versus total intensity calculated for the phasors shown in (b). (d) Analysis of the dependence of mean phase lifetime $\langle \tau \rangle$ and standard deviation σ_τ on total intensity (expressed in counts/pixel). The latter is well described by a power law with exponent $a = -0.45$, consistent with shot noise-limited measurement. (g) Phase lifetime histogram corresponding to the phasor plot shown in (f) and fit with a Gaussian (red curve), from which a peak phase lifetime and standard deviation are extracted. (h) Peak phase lifetime (black circles) and SDV (red squares) of the 10 μM Cy3B sample, computed as described in (g), as a function of phantom thickness. For all samples, the average fluorescence intensity per pixel was around 30 000 counts. The phase lifetime SDV of the Cy3B sample observed without phantom (0 mm) was obtained by extrapolating the curve obtained in (d). The straight lines correspond to the linear fits.
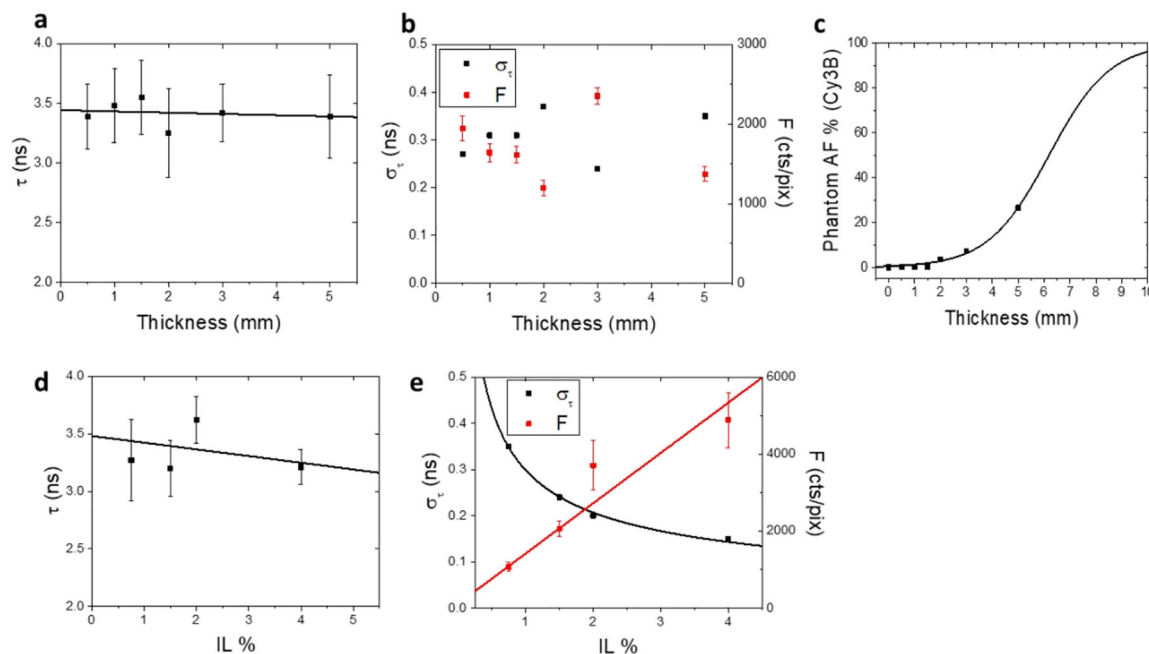
Figure 3.
Phasor analysis of phantom AF. (a) The average AF phase lifetime measured for all thicknesses is essentially independent from thickness (the linear fit gives a slope of 10.6 ps/mm). Error bars are the standard deviations calculated by a Gaussian fitting of the phase lifetime histograms, as explained in Figure 2g. (b) AF phase lifetime standard deviation (SDV, black dots) of the six phantom layers and total fluorescence signal (red dots) are independent from thickness. The constant SDV mirroring the constant fluorescence intensity is consistent with an SDV dominated by shot noise. (c) The measured phantom AF count rate can be used to estimate the contribution of AF to the Cy3B signals studied in Figure 2. Its contribution is negligible below 2 mm but reaches 27% for the 5 mm phantom. The model fitted to the data is discussed in the text. (d) AF phase lifetime for 0.5 mm phantoms with different intralipid (IL) fractions, showing very little dependence on IL concentration (the linear fit has a slope of 58 ps/%). (e) AF phase lifetime standard deviation and AF fluorescence intensity of the four phantom layers studied in (d). The AF intensity (red dots) increases linearly with intralipid concentration, which is accompanied by a decrease of the phase lifetime SDV (black dots) as $I^{-0.53}$, expected in the case of a pure shot noise dependence.
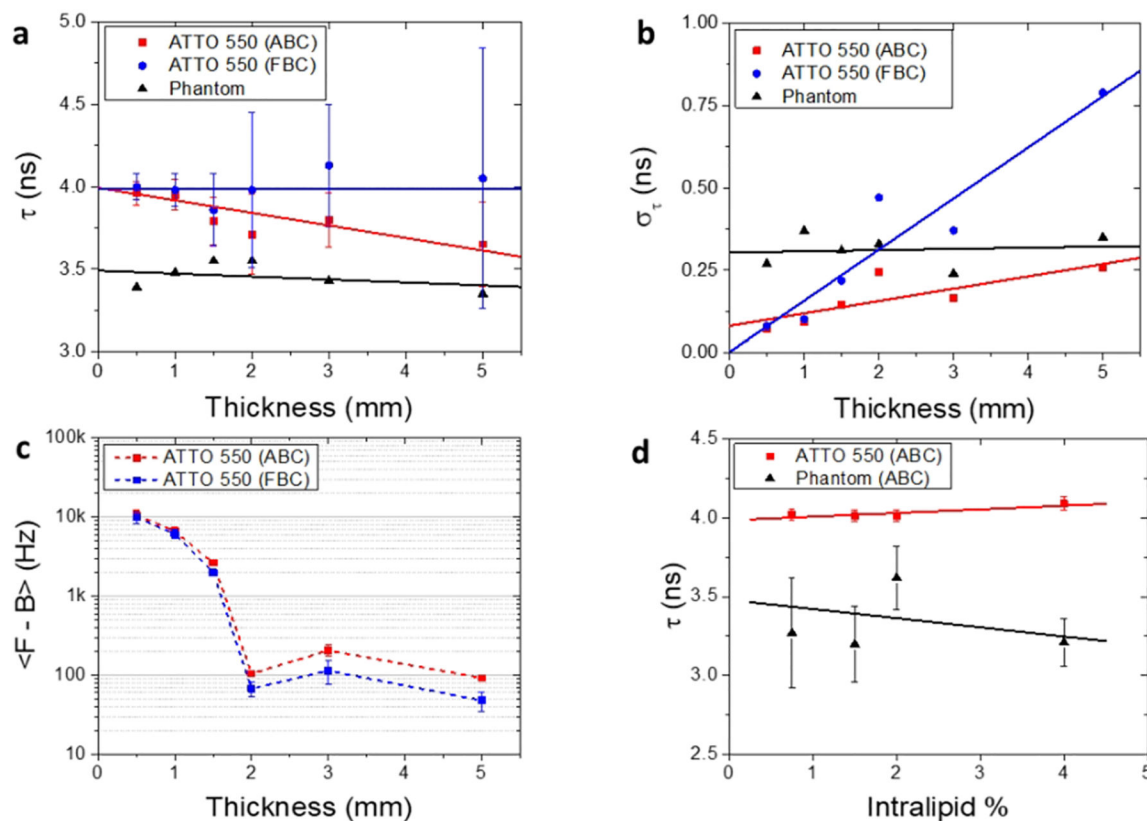
Figure 4.
(a) Phase lifetime of the ATTO 550 sample observed behind phantoms of different thicknesses, calculated by the analytical background correction (ABC, red curve) or by subtracting the phantom only signal (file background correction, FBC, blue curve). The black symbols correspond to the phase lifetimes of the pure phantom samples used as background files. Error bars are the standard deviations calculated by Gaussian fitting of the phase lifetime histograms, as explained in Figure 2g. (b) Phase lifetime standard deviation (SDV, shown in (a) as error bars) as a function of phantom thickness. The phantom-only phase lifetime SDV (black symbols) is essentially constant. The SDV of the phase lifetime calculated by numerical estimation of the ABC (red curve) triples from 0.5 mm and 5 mm samples, while that estimated by phantom-only data subtraction (FBC, blue curve) is almost tenfold higher for the 5 mm sample compared to the 0.5 mm sample, which reflects the lower signal intensity achieved by phantom BG subtraction. (c) Count rate (per 4×4 pixel ROI) as a function of phantom thickness. The sample's fluorescence decreases exponentially with increasing thickness. In the absence of AF correction (red curve), the total signal used for phase lifetime calculation is larger, especially for the thicker phantom layers (2, 3 and 5 mm thick phantoms) explaining the smaller standard deviation shown in (b). Error bars (often smaller than the symbols) indicate standard deviation. (d) Phase lifetime of ATTO 550 behind 0.5 mm phantom layer (red) and the AF of 0.5 mm phantom layers (black, from Figure 3d) with increasing intralipid concentrations (0.75, 1.5, 2 and 4%). ATTO 550 phase lifetime calculations were performed using software background subtraction. ATTO 550's

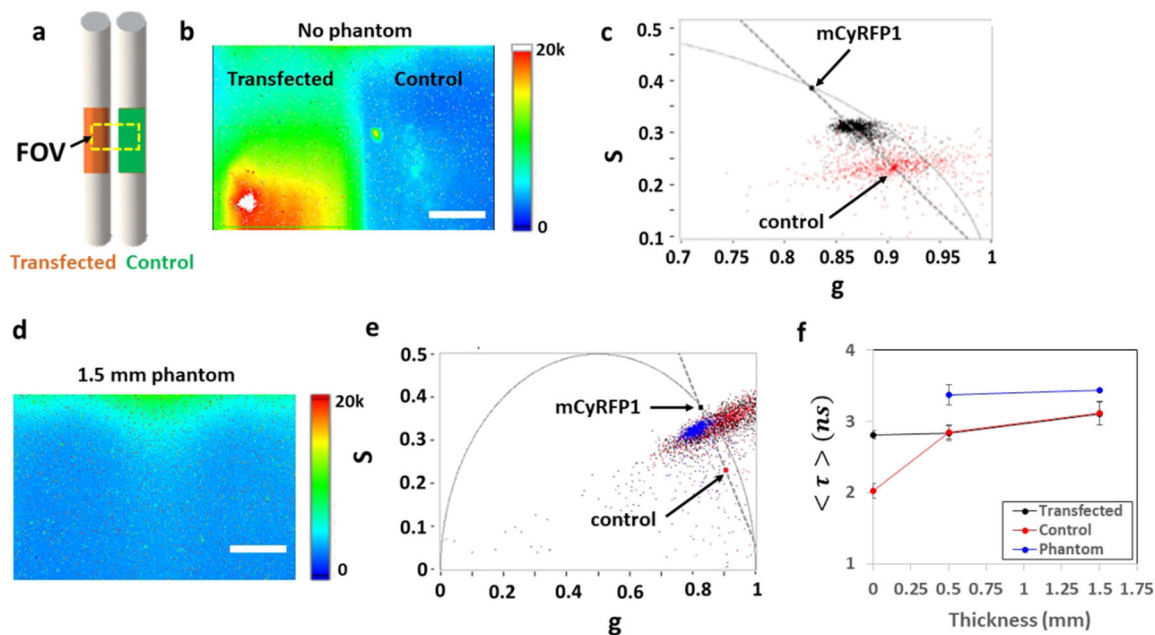phase lifetime remains distinct from that of the phantom AF. The straight lines correspond to linear fits.

Figure 5.
Fluorescence phase lifetime analysis of A549 cells expressing the fluorescent protein mCyRFP1 behind phantom layers 0.5 and 1.5 mm in thickness. (a) Schematic illustration of the experimental layout: two adjacent capillaries, loaded with mCyRFP1-transfected A549 cells (left, orange rectangle) and untransfected (control) A549 cells (right, green rectangle), were simultaneously recorded for FLI analysis. FOV: field of view as was recorded by the detector. (b) Fluorescence image of the adjacent capillaries illustrated in (a). The transfected cells are characterized by a bright fluorescence, resulting from the expressed mCyRPFP1 protein, while the control cells emit a lower intensity resulting from AF. Scale bar is 160 μm. (c) Phasor scatterplots for the two sides of the fluorescence image presented in (b), corresponding to the control (red scatterplot) and transfected A459 cells (black scatterplot) without phantom, showing two distinct average phase lifetimes of 2.0 and 2.8 ns, respectively. The black dot at the intersection of the UC and the dashed gray segment has a lifetime of 3.4 ns, corresponding to the literature value of mCyRFP1 (see ref 32). The dashed line connects this point to the barycenter of the control cells' scatterplot (red dot). The alignment of the transfected cells' scatterplot with this line is because its fluorescence is composed of a similar amount of cell AF (red dot) and mCyRFP1 fluorescence (black dot). (d) Fluorescence images for transfected A549 and control cells, behind a 1.5 mm phantom. Scale bar is 160 μm. (e) Phasor scatterplots of the two samples behind a 1.5 mm phantom and of the phantom layer. A marked jump of the phasor scatterplot of the region occupied by control cells (red dots) is noticeable. The resulting phasor scatterplot is almost identical to that of the region occupied by the transfected cells (black dots), whose photons are scattered throughout the whole image. The phasor scatterplot of the transfected cells shows a negligible change compared to (c), with a small move toward the phantom's phase lifetime (3.4 ns, blue dots), coincidentally similar to the lifetime of mCyRFP1. (f) Phase lifetime of A549 cells expressing mCyRP1 (black curve), control A549 cells (red curve), and phantom AF (blue line). The sample containing the control cells (AF phase lifetime: 2.1 ns)

has a phase lifetime that is indistinguishable from that of the transfected cells as soon as it is observed behind any amount of phantom, while the cells expressing an FP exhibited a moderate increase in their lifetime, which is still distinguishable from the phantom lifetime for all phantom thicknesses.